# Laser-driven electron acceleration in nanoplate array targets

A. R. Knyazev, Y. Zhang, and S. I. Krasheninnikov
*University of California San Diego, La Jolla, California 92093-0411, USA*

(Received 16 September 2020; accepted 8 December 2020; published 8 January 2021)

This paper proposes a model of the laser-driven electron acceleration that occurs when a high-intensity laser interacts with a nanoplate target. It shows that quasistatic electric $\mathbf{E}_{qs}$ and magnetic $\mathbf{B}_{qs}$ fields can be formed when the laser, polarized normal to the nanoplates, extracts electrons from the nanoplates. Considering the physical natures of $\mathbf{E}_{qs}$ and $\mathbf{B}_{qs}$, the amplitude of $\mathbf{E}_{qs}$ is relatively larger than $\mathbf{B}_{qs}$. Such a residual between static electric and magnetic field is shown to be crucial for the electron acceleration beyond the ponderomotive scaling, as it can cause onset of stochastic electron motion. The analysis demonstrates that the maximum electron energy in units of ponderomotive scaling depends on a single universal parameter, which is composed of laser amplitude, spacing between nanoplates, and electron initial conditions. The analytical results are confirmed by a series of two-dimensional particle-in-cell simulations using EPOCH code.

DOI: 10.1103/PhysRevE.103.013204

## I. INTRODUCTION

Interaction of high-intensity lasers with solid targets can result in a high yield of both x-rays and energetic electrons. To efficiently convert the energy of the incident laser into the energy of the radiated x-rays and emitted electrons, it is necessary that the target absorbs most of the incident laser energy. Multiple studies [1,2] indicate that flat targets typically absorb less than 10% of the laser pulse energy, while structured targets can absorb over 90%. Laser interaction with different structured targets, such as nanorod arrays [2], "velvet" targets [3], "smoked" targets [4], and "foamed" targets [5], were studied experimentally and via computer simulations. However, the physics of the electron acceleration during the laser-target interaction is not yet completely described. It was shown [6] that the interaction of the microchannel target with the laser creates the quasistatic electric fields in the cavities of the target. The presence of static electric and magnetic fields can lead to the stochastic acceleration of the electrons by the laser, as was demonstrated [7–9] with the Hamiltonian formalism.

In this paper, we model the interaction of a laser with a periodic nanoplate array target. We show that quasistatic electric $\mathbf{E}_{qs}$ and magnetic $\mathbf{B}_{qs}$ fields can emerge in such setup, and develop a semianalytic model for the formation of such fields. We use the 3/2-dimensional Hamiltonian [9] formalism to describe the motion of a single electron in the presence of the laser and prescribed $\mathbf{E}_{qs}$ and magnetic $\mathbf{B}_{qs}$ fields. From the single-electron model, we find the condition for the onset of stochastic electron heating. We also determine when the maximum electron energy $\mathcal{E}_{max}$ from stochastic heating exceeds ponderomotive energy scaling [10]. We verify our analytic results with a series of two-dimensional particle-in-cell (2D PIC) simulations. The maximum electron energy in our PIC simulations can be explained with the proposed stochastic acceleration mechanism.

The rest of the paper is organized as follows. In Sec. II we describe the simulation setup. Extraction of the electrons from the target by the laser pulse and formation of the quasistatic electromagnetic fields are analyzed in Sec. III. In Sec. IV we examine the acceleration of electrons in the laser and quasistatic fields. The results of PIC simulations are presented in Sec. V. Section VI is the conclusion.

## II. SETUP DESCRIPTION

Laser-target interaction experiments typically involve complex, often irregular structures. Direct simulation of such structures requires a three-dimensional (3D) consideration [5,11,12], which poses significant computational challenges. Modeling complex structures can also make it hard to pinpoint important physics mechanisms. In this work, we consider a simplified 2D model of a nanoplate target as shown in Fig. 1. We model the target by filling a region of the simulation domain with a cold plasma, as shown with black in Fig. 1. The nanoplates of the target are modeled as rectangular regions with a length of sides $d = 0.1\lambda$ along $\mathbf{e}_y$, and $L = 20\lambda$ along $\mathbf{e}_z$, where $\lambda = 400$ nm is the wavelength of the incident laser pulse propagating along $\mathbf{e}_z$. The backplate of the target is modeled as a slab of size $L_{bp} = \lambda$ along $\mathbf{e}_z$. The gaps between neighboring nanoplates are all equal to $D$, with different values of $D$ from $0.25\lambda$ to $12\lambda$ considered in our series of PIC simulations. The material of a target is modeled by a cold plasma, composed of immobile ions pre-ionozed to an arbitrarily chosen value $Z = 5$, and the electrons. The number density of the electrons is set to $n_e = 50n_{cr}$, where $n_{cr} = m\omega^2/4\pi e^2 = 6.97 \times 10^{21}\,\mathrm{cm}^{-3}$ is the critical plasma density, $m$ is the electron mass, $e$ is the electron charge, and $\omega = 2\pi c/\lambda$ is the laser frequency. The number density of ions is set to $n_i = n_e/Z \approx 6 \times 10^{22}\,\mathrm{cm}^{-3}$, which is similar to the number density of ions in solid copper.

The laser consists of a $2\lambda$ long prepulse, followed by a $15\lambda$ long main pulse and a $2\lambda$ decay, as shown in Fig. 1.

 

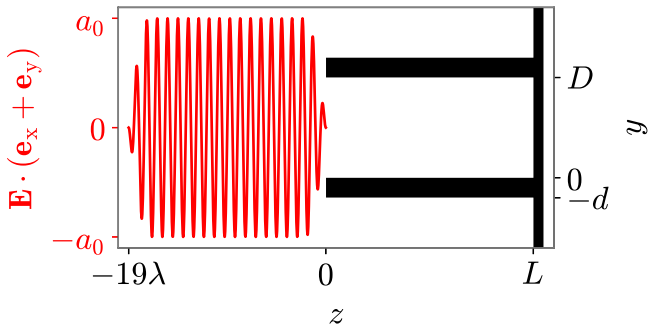


FIG. 1. Schematic view of the simulation setup. The black region corresponds to where the target is located in the domain. The nanoplates are separated by vacuum gaps of width $D$. Each nanoplate has the width $d$ along the $y$-axis and length $L$ along the $z$-axis. Nanoplates are connected on the right side at $z = L$ with the bulk of width $\lambda$. Top and bottom boundaries of the simulation domain are periodic, left and right boundaries are open. The laser pulse arrives from the left boundary. The electric field of the laser at time $t = 0$ is shown by the red curve at $z$ between $-19\lambda$ and 0.

The main pulse is described by a vector potential $\mathbf{a}$ of magnitude $a = -a_0 \cos(\xi)$, where $a_0 = eE/mc\omega$ is the normalized vector potential, $\xi = \omega(t - z/c)$, and $c$ is the speed of light in vacuum. We considered two laser polarizations, described by $\mathbf{a} = a\mathbf{e}_x$ ($x$-polarized) and $\mathbf{a} = a\mathbf{e}_y$ ($y$-polarized). The value of $a_0$ ranged from 1.0 to 4.0, corresponding to laser intensities from $1.8 \times 10^{19}$ W/cm$^2$ to $1 \times 10^{20}$ W/cm$^2$. We chose the frame of reference so that the laser prepulse reaches the nanoplates at $z = 0$ at time $t = 0$, as shown in Fig. 1.

We conduct our PIC simulations with the fully relativistic 2D3V PIC code EPOCH [13]. The simulation domain has the size $2d + 2D$ along the $y$-axis and $31\lambda + L$ along the $z$-axis. Each cell has a size of $0.01\lambda$ along both the $y$- and $z$-axes. Boundaries normal to the $y$-axis are periodic for both particles and fields. Boundaries normal to the $z$-axis are open for both particles and fields.

The rest of this paper uses normalized units marked with a hat. Distances are normalized by $\lambda/2\pi$. Velocities of electrons are normalized by the speed of light $c$. Number densities are normalized by $n_{cr}$. Time is normalized by $1/\omega$. The momentum of electrons is normalized by $mc$. The magnitudes of the electric and magnetic fields are normalized by $mc\omega/e$. Potentials of electric and magnetic fields are normalized by $mc^2/e$. Electric currents are normalized by $en_{cr}c$.

### A. Role of the laser polarization

Polarization of the laser pulse significantly affects the laser-target interaction. In the rest of this section, we will show that the $y$-polarized pulse can propagate into the gap of any size $\hat{D}$, while the $x$-polarized pulse is reflected if $\hat{D} < \pi$. Furthermore, as will be discussed in Sec. III, only the $y$-polarized pulse creates the quasistatic fields inside the gap.

Because of the high conductivity of nanoplates, we can approximate them as ideal conductor and explain the difference between $x$ and $y$ polarization of a laser with a simple model of a lossless multiconnected waveguide. Specifically, consider the waveguide formed by two parallel, ideally conducting plates located at $\hat{y} = 0$ and $\hat{y} = \hat{D}$. Such waveguide has three types [14] of $\mathbf{E}, \mathbf{B} \propto \exp[i(\hat{t} - \hat{z})]$ modes: purely transverse (TEM) modes, modes with longitudinal components of the electric field (TM modes), and modes with longitudinal components of magnetic field (TE modes). Due to $E_x = 0$ boundary conditions, TEM modes in such a waveguide can be polarized only along $\mathbf{e}_y$ and have the same electric and magnetic fields as a plane wave. Furthermore, TEM modes can propagate in a gap of any size $\hat{D}$ and have luminal phase velocity. The electric field of such a TEM mode is normal to the waveguide boundary, and therefore it can extract electrons from the boundary by the electric force.

Meanwhile, the only $x$-polarized modes in the aforementioned waveguide are TE modes. The dispersion relation for TE modes suggests $\omega \geqslant c\pi/D$, therefore TE modes can propagate only in a gap $\hat{D} > \pi$. As a crude model for the propagation of the $x$-polarized pulse inside the gap, one can Fourier expand the plane wave at the gap entrance $|\mathbf{E}| = |E(y, z = 0)\mathbf{e}_x| = \tilde{E}_x = \text{const}$ into a sum of TE modes. The resulting expansion of $\tilde{E}_x$ gives $E_{TE} = \alpha_l E_{x,l}$, where

$$\alpha_l = \frac{2\tilde{E}_x[1 - \cos(\pi l)]}{\pi l}, \quad E_{x,l} \propto \sin\left(\pi l \frac{y}{D}\right), \tag{1}$$

and $l$ is an integer. The expression for the $z$-component of magnetic field $B_{TE}$ is $B_{TE} = \alpha_l B_{z,l}$, where $B_{z,l}$ is the $z$-component of magnetic field of the TE mode with electric field $E_{x,l}\mathbf{e}_x$.

Electrons subjected to $E_{TE}\mathbf{e}_x$ and $B_{TE}\mathbf{e}_z$ experience the ponderomotive force pushing the electrons from the gap into the plasma, where there is no laser field and therefore no efficient electron acceleration. Since this paper focuses on laser-driven electron acceleration, in the rest of the paper we will primarily study the $y$-polarization case.

## III. ELECTRON EXTRACTION AND FORMATION OF QUASISTATIC ELECTROMAGNETIC FIELD

As the $y$-polarized pulse propagates between the nanoplates, it extracts some of the electrons from them. The extracted electrons can then either return to their parent nanoplate or stream away from it depending on the laser phase. The counterpropagating bunches of streaming electrons with a laser phase difference of $\pi$, extracted from the opposite boundaries of the gap between nanoplates, eventually pass through each other, mix up, and form an approximately homogeneous electron density $\bar{n}$ in the gap.

To have some understanding of extraction process we consider the following model. We consider the electron located at the boundary between the nanoplate and the gap. We also assume that the field acting on this electron is the same as the field of a plane wave, propagating along the surface of the nanoplate. Specifically, we consider a motion of a single electron in the plane wave described by a vector potential $-a_0 \cos(\xi + \xi_0)\mathbf{e}_y$, where $\xi_0$ is the phase of the plane wave at the moment of electron extraction. The electron is assumed to be initially immobile. The motion of an initially immobile electron in a plane EM wave has three well-known integrals of motion:

$$\hat{p}_x = 0, \quad \hat{p}_y + a_0 \cos(\xi + \xi_0) = a_0 \cos(\xi_0), \quad \gamma - \hat{p}_z = 1, \tag{2}$$

where $\gamma^2 = 1 + \hat{\mathbf{p}}^2$. Without loss of generality we set the $y$-coordinate of the nanoplate surface from which the electron is extracted to $\hat{y}_0 = 0$. From Eqs. (2), it follows that

$$\frac{d\hat{y}}{d\xi} = a_0[\cos(\xi_0) - \cos(\xi + \xi_0)]. \tag{3}$$

Equation (3) shows that only specific values of the initial phase $\xi_0$ lead to the extraction of the electron into the gap. Indeed, if the gap is in the $\hat{y} < 0$ region, the electron is extracted only if $\sin(\xi_0) > 0$. Likewise, for the gap in $\hat{y} > 0$ region, the electron is extracted if $\sin(\xi_0) < 0$. From Eqs. (2) we can derive the equations for electron's trajectory,

$$\hat{y} = a_0[\xi\cos(\xi_0) + \sin(\xi_0) - \sin(\xi + \xi_0)], \tag{4}$$

$$\hat{z} - \hat{z}_0 = \frac{a_0^2}{2}\left\{\xi\left[1 + \frac{1}{2}\cos(2\xi_0)\right] + \frac{1}{4}\sin[2(\xi + \xi_0)] - \sin(\xi) - \sin(\xi + 2\xi_0)\right\}, \tag{5}$$

where $\hat{z}_0$ is the $z$-coordinate of the electron before the extraction. From Eq. (4) we conclude that depending on the phase $\xi_0$ the extracted electron may either return to its parent nanoplate or stream away from it. The electron bunches that stream along the $y$-axis have a phase difference of $\Delta\xi = \pi$ with the electron bunches that stream in the opposite direction. From Eqs. (4) and (5), we can estimate the maximum angle $\theta$ between the radius vector of the electron and the $y = 0$ boundary as

$$\lim_{\xi\to\infty}\frac{\hat{y}(\xi)}{\hat{z}(\xi) - \hat{z}_0} = \frac{4\cos(\xi_0)}{a_0[2 + \cos(2\xi_0)]} < \frac{\sqrt{2}}{a_0} = \tan(\theta). \tag{6}$$

The estimate given by Eq. (6) neglects the effect of the Coulomb forces between the extracted electrons and the parent nanoplate and therefore is accurate only for extracted electrons with small $\hat{y}$. As extracted electrons move away from the parent nanoplate, the value of the streaming angle $\theta$ becomes less than predicted by Eq. (6).

As bunches of the electrons propagate away from their parent nanoplates along the $y$-axis, they eventually meet a bunch of counterpropagating electrons. From Eq. (6), we conclude that the length $\hat{L}$ of the gap needs to be at least $\hat{L} > a_0\hat{D}/\sqrt{2}$ for the first extracted bunches of electrons to start mixing with the counterpropagating bunches. When the mixing occurs, mixed electron bunches form the homogeneous electron density $\bar{n}$ inside the gap. The charge density inside the gap creates the electric field $\mathbf{E}_{\rm qs}$. The current of the extracted electrons in the gap $\hat{j} = \hat{\bar{n}}\hat{v}_z$ creates the magnetic field $\mathbf{B}_{\rm qs}$. Velocity $\hat{v}_z$ can be estimated from Eqs. (2) as

$$\hat{v}_z = \frac{\hat{p}_y^2}{2 + \hat{p}_y^2} \sim \frac{a_0^2}{2 + a_0^2}. \tag{7}$$

Since $\hat{v}_z < 1$, the magnitude of the magnetic field $B_{\rm qs}$ is weaker than the magnitude of the electric field $E_{\rm qs}$. In Sec. IV we will show that the difference between $E_{\rm qs}$ and $B_{\rm qs}$ is important for the onset of stochastic electron acceleration.

Assuming that electron extraction stops when the electric field $\mathbf{E}_{\rm qs}$ from the electrons in the gap compensates for the electric field of the laser pulse at the boundary, the density of the electrons $\hat{\bar{n}}$ after mixing can be estimated as

$$\hat{\bar{n}} = \frac{2a_0}{\hat{D}}. \tag{8}$$

The analysis above assumes ions are immobile. Mobile ions will expand into the $\hat{D}$ gap when subjected to the $\mathbf{E}_{\rm qs}$ field, closing the gaps between nanoplates. For nonrelativistic ion motion the time $\tau_i$ to cross the gap $\hat{D}$ is $\tau_i \sim \sqrt{2\hat{D}\hat{m}_i/Za_0}$, where $\hat{m}_i$ is the ion mass in units of electron mass. Therefore, our immobile ion analysis with the $y$-polarized pulse will be applicable only during times shorter that $\hat{\tau}_i$. For the copper target with parameters from Sec. II, $\hat{\tau}_i > 100$ and the immobile ions assumption holds. In our PIC simulations with a $y$-polarized laser, the time it takes for the laser pulse to reach the back wall is less than $\tau_i$ and hence the immobile ions assumption applies. For larger $a_0 \sim 100$ the motion of ions can no longer be neglected for practical $\hat{D} \sim 10$ gap sizes.

Concluding this section, we note the differences of the quasistatic electric and magnetic fields in the gap from the quasistatic fields in another laser-plasma interaction setup, the evacuated ion channel [15]. As a matter of fact, the quasistatic electric and magnetic fields in the gap can be called "electron" channel, where the $\mathbf{E}_{\rm qs} \times \mathbf{B}_{\rm qs}$ force is along the direction of laser propagation, whereas, in the ion channel, the $\mathbf{E}_{\rm qs} \times \mathbf{B}_{\rm qs}$ force is directed against the laser propagation.

## IV. STOCHASTIC ACCELERATION

In this section we examine the electron acceleration in laser and quasistatic fields. Based on the results from Sec. III, fields $\hat{\mathbf{E}}_{\rm qs}$ and $\hat{\mathbf{B}}_{\rm qs}$ between two neighbor nanoplates can be described with scalar $\hat{U}(\hat{y})$ and vector $\hat{A}_{\rm B}(\hat{y})$ potentials as $\hat{\mathbf{E}}_{\rm qs} = \boldsymbol{\nabla}\hat{U}(\hat{y})$ and $\hat{\mathbf{B}}_{\rm qs} = -\boldsymbol{\nabla} \times (\hat{A}_{\rm B}\mathbf{e}_z)$, where

$$\hat{U}(\hat{y}) = \frac{\kappa_U}{2}\left[\frac{\hat{D}^2}{4} - \left(\hat{y} - \frac{\hat{D}}{2}\right)^2\right], \tag{9}$$

$$\hat{A}_{\rm B}(\hat{y}) = \frac{\kappa_{\rm B}}{2}\left[\frac{\hat{D}^2}{4} - \left(\hat{y} - \frac{\hat{D}}{2}\right)^2\right], \tag{10}$$

where $\kappa_U = \hat{\bar{n}}$ and $\kappa_{\rm B} = \kappa_U\hat{v}_z$. The signs of $\hat{U}$ and $\hat{A}_{\rm B}$ defined in (9) and (10) are chosen to be positive so they are opposite to the conventional electrostatic and vector potential. In the rest of the section, we will neglect the size of each nanoplate $\hat{d} = 0$, so the structure of the $\hat{\mathbf{E}}_{\rm qs}$ and $\hat{\mathbf{B}}_{\rm qs}$ fields in the target is described by a chain of $\hat{U}(\hat{y})$ and $A_{\rm B}(\hat{y})\mathbf{e}_z$ potentials defined in (9) and (10). The motion of a single electron in the presence of the $\hat{\mathbf{E}}_{\rm qs}$ and $\hat{\mathbf{B}}_{\rm qs}$ fields and the laser wave with vector potential $\mathbf{a} = -a_0\cos(\xi)\mathbf{e}_y$ is described by a 3/2-dimensional Hamiltonian [8] as

$$\frac{d\hat{P}_y}{d\xi} = -\frac{\partial\hat{H}}{\partial\hat{y}}, \quad \frac{d\hat{y}}{d\xi} = \frac{\partial\hat{H}}{\partial\hat{P}_y}, \tag{11}$$

$$\hat{H} = \frac{1}{2}\left\{\frac{1 + [\hat{P}_y - a_0\cos(\xi)]^2}{C - W^{(-)}(\hat{y})} + W^{(+)}(\hat{y}) + C\right\}, \tag{12}$$

$$W^{(\pm)}(\hat{y}) = \hat{U}(\hat{y}) \pm \hat{A}_{\rm B}(\hat{y}), \tag{13}$$

$$C = \gamma + W^{(-)}(\hat{y}) - \hat{p}_z = \text{const}, \tag{14}$$

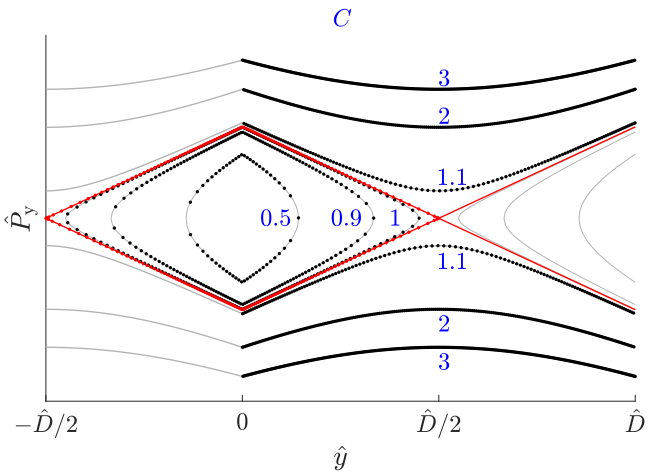


FIG. 2. Unperturbed trajectories of energetic electrons (17) for $\hat{H} = 50$, $W_{\max}^{(-)} = 1$, and various values of $C$. Red lines that cross at $\hat{D}/2$ show the trajectory with $C = 1/2\hat{H} + W_{\max}^{(-)} = 1.01$, separating bounded and unbounded trajectories. Dots show the stroboscopic portrait of the motion.

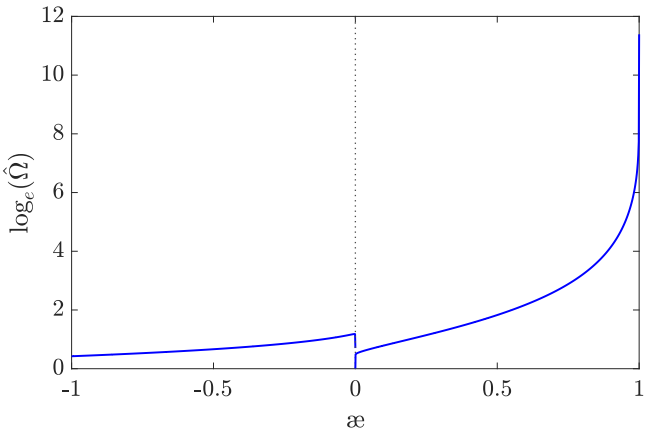


FIG. 3. Frequency $\hat{\Omega} = (d\hat{H}/d\mathcal{I})$ of unperturbed electron motion (17) for $\hat{H} = 50$, $W_{\max}^{(-)} = 2$, $\hat{D} = 8\pi$, and various æ values. The bifurcation at æ=0 corresponds to the separatrix, where $\hat{\Omega} = 0$.

where $\hat{P}_y = \hat{p}_y + a_0\cos(\xi)$ is the canonical momentum, and $\hat{p}_x = \text{const}$ is set as zero. The Hamiltonian (12) is equal to the total electron energy $\hat{H} = \gamma + \hat{U}$. Without the laser $a_0 = 0$, the energy is conserved $\hat{H} = \text{const}$ and the corresponding unperturbed electron motion is periodic with some frequency $\hat{\Omega}$. To heat the electron efficiently, the laser pulse has to resonate with the harmonics of unperturbed electron, motion [16] which is possible only for $\hat{\Omega} < 1$. For $\hat{\Omega} < 1$, the resonances of laser with harmonics of electron motion can occur, and overlap of such resonances enables stochastic acceleration.

Stochastic electron motion can be imagined as a series of "kicks" separated by adiabatic motion. These kicks can lead to stochasticity [9] if

$$K \approx \left|\frac{\partial \hat{T}_e}{\partial \hat{H}}\Delta\hat{H}\right| \gtrapprox 1, \tag{15}$$

where $\hat{T}_e = 2\pi/\hat{\Omega}$ and $\Delta\hat{H}$ are, respectively, the time and change of electron Hamiltonian between two consecutive kicks. In this section we will use condition (15) to estimate the maximum energy of the stochastic electron motion.

Since we are interested in energetic electrons, we consider

$$\hat{H} \gg \max\left(1, C, W_{\max}^{(+)} = \frac{\kappa_U + \kappa_B}{8}\hat{D}^2\right). \tag{16}$$

Using Eq. (8), we estimate $W_{\max}^{(+)} \sim a_0\hat{D}/2$. Under assumption (16), the Hamiltonian (12) can be approximated as

$$\hat{H} \approx \frac{1}{2}\left\{\frac{1 + [\hat{P}_y - a_0\cos(\xi)]^2}{C - W^{(-)}(\hat{y})}\right\}. \tag{17}$$

Unperturbed trajectories described by (17) are shown in Fig. 2. These unperturbed trajectories are bounded if $C < 1/2\hat{H} + W_{\max}^{(-)}$, where $W_{\max}^{(-)} = (\kappa_U - \kappa_B)\hat{D}^2/8$, and unbounded otherwise.

To examine the unperturbed motion frequency $\hat{\Omega}$ of bounded and passing electrons, we use action-angle variables $(\mathcal{I}, \vartheta)$. Let æ$= ((2\hat{H})^{-1} + W_{\max}^{(-)} - C)/W_{\max}^{(-)}$ characterize the distance form the electron's trajectory to the separatrix, in a range from $-\infty$ to 1. Indeed, æ=0 corresponds to the separatrix, æ>0 is bounded motion, æ=1 is the equilibrium point at $\hat{y} = 0$, $\hat{P}_y = 0$, and negative æ correspond to passing trajectories. For bounded motion, $2\pi\mathcal{I} = \oint \hat{P}_y\, d\hat{y}$, and for the passing electrons $2\pi\mathcal{I} = \int_{\hat{y}}^{\hat{y}+\hat{D}} \hat{P}_y\, d\hat{y}$. The frequency is calculated as $\hat{\Omega} = (d\mathcal{I}/d\hat{H})^{-1}$, and the resulting $\hat{\Omega}$(æ) dependence is shown in Fig. 3. As æ goes to zero, the frequency $\hat{\Omega}$ also goes to zero. Transformation to canonical variables allows us to determine how $\hat{\Omega}$ depends on $W_{\max}^{(-)}$, $\hat{D}$, and particle energy $\hat{H}$. We will get these dependencies in an easier way later in this section. We will now determine the maximum stochastic energies for the cases when unperturbed electron motion is unbounded $C \gg W_{\max}^{(-)}$, close to separatrix $C \sim W_{\max}^{(-)}$, and bounded $C \ll W_{\max}^{(-)}$.

For the $C \gg W_{\max}^{(-)}$ case, Hamiltonian (17) can be approximated as

$$\hat{H} \approx \hat{H}_1 = \frac{1}{2}\left\{\frac{1 + [\hat{P}_y - a_0\cos(\xi)]^2}{C}\right\}, \tag{18}$$

which is equivalent to the Hamiltonian (12) for the ponderomotive acceleration $\hat{A}_B = \hat{U} = 0$ case. Hamiltonian (18) corresponds to linear equation of motion, meaning that no stochasticity is possible. Another way to see that the system with Hamiltonian (18) has no stochasticity is to note that the spectra of the oscillations described by Hamiltonian (18) consist of a single harmonic, and therefore a Chirikov's resonance overlap criterion cannot be satisfied. Ponderomotive acceleration $\hat{\mathcal{E}}_{\text{pond}} = a_0^2/C$ described by Hamiltonian (18) is efficient only for the small dephasing rate $\gamma - \hat{p}_z \ll 1$. But if the dephasing rate is small, then from (14) we conclude that $C \sim W^{(-)}(\hat{y})$, which contradicts the $C \gg W_{\max}^{(-)}$ condition. Therefore, in the $C \gg W_{\max}^{(-)}$ case no stochastic acceleration occurs and the electron acceleration is inefficient.

For $C \approx W_{\max}^{(-)}$, Eq. (17) illustrates that the resonant points are $|\hat{y}| \approx \hat{D}/2$. It is convenient to rewrite Eq. (17) as

$$\frac{4W_{\max}^{(-)}}{\hat{D}^2}\left(\hat{y} - \frac{\hat{D}}{2}\right)^2 - \frac{\hat{P}_y^2}{2\hat{H}_2} \approx W_{\max}^{(-)} - C. \tag{19}$$

Therefore, for $C \approx W_{\max}^{(-)}$, Eq. (19) describes two lines, one of which is

$$\hat{P}_y = \frac{\sqrt{8\hat{H}_2 C}}{\hat{D}}\left(\hat{y} - \frac{\hat{D}}{2}\right). \tag{20}$$

From Eqs. (11) and (20) we get the equation of unperturbed electron motion

$$\sqrt{\frac{C}{2\hat{H}_2}}\frac{1}{\hat{D}}\left(\hat{y} - \frac{\hat{D}}{2}\right)^2 = \xi - \xi_{\max}, \tag{21}$$

where $\xi_{\max}$ is when an electron is at $\hat{y} = \hat{D}/2$. For $C$ slightly less than $W_{\max}^{(-)}$ the electron trajectory is bounded, and it takes a quarter of the period $\hat{T}_2$ of the electron's motion to go from $\hat{y} = 0$ to $\hat{y} = \hat{D}/2$. We can estimate $\hat{T}_2$ as

$$\hat{T}_2 = \sqrt{\frac{C}{2\hat{H}_2}}\hat{D} \propto \frac{\zeta \hat{\mathcal{E}}_{\text{pond}}^{1/2}}{\hat{H}_2^{1/2}}, \tag{22}$$

and hence the frequency of motion is $\hat{\Omega}_2 \sim \hat{D}\sqrt{\hat{H}_2/C}$. Stochastic heating requires overlapping of high harmonics resonance and thus $\hat{\Omega}_2 \ll 1$. Therefore, the maximum energy scaling we should expect is $\hat{H}_2 < C\hat{D}^2$ ($\hat{\Omega}_2 \approx 1$). If it exceeds the ponderomotive scaling $\hat{\mathcal{E}}_{\text{pond}}$, we have

$$\frac{a_0^2}{C} \leqslant C\hat{D}^2 \Leftrightarrow \zeta \equiv \frac{\hat{D}C}{a_0} > 1. \tag{23}$$

We can use Eqs. (11) and (20) to estimate change $\Delta\hat{H}_2$ of the electron's energy during $\hat{T}_2$ in the presence of the laser as

$$\Delta\hat{H}_2 = \int \frac{\partial \hat{H}_2}{\partial \xi}\frac{d\xi}{d\hat{y}}d\hat{y} \propto \left(\hat{H}_2 \zeta^2 \hat{\mathcal{E}}_{\text{pond}}^3\right)^{1/4}. \tag{24}$$

Therefore, the maximum energy of stochastic motion is determined by

$$K = \left|\frac{\partial \hat{T}_2}{\partial \hat{H}_2}\Delta\hat{H}_2\right| \sim \zeta^{3/2}\left[\frac{\hat{\mathcal{E}}_{\text{pond}}}{\max(\hat{H}_2)}\right]^{5/4} = 1, \tag{25}$$

where we used estimates (22) and (24). From Eq. (25) we determine the scaling of $\max(\hat{H}_2)$ to be

$$\max(\hat{H}_2) \propto \hat{\mathcal{E}}_{\text{pond}}\zeta^{6/5}. \tag{26}$$

For $C \ll W_{\max}^{(-)}$, from Eq. (12) we know that the electron motion is bound to $\hat{y} \ll \hat{D}$, so we can approximate Hamiltonian (17) as

$$\hat{H}_3 = \frac{1}{2C}\left\{\frac{1 + [\hat{P}_y - a_0\cos(\xi)]^2}{1 - \alpha|\hat{y}|}\right\}, \tag{27}$$

where $\alpha = 4W_{\max}^{(-)}/C\hat{D}$. It follows that the resonant points are $|\hat{y}| \approx 1/\alpha$. From Hamiltonian (27) we find the equation of unperturbed electron motion from (11) to be

$$\sqrt{\frac{2C}{\hat{H}_3}}\frac{2}{3\alpha}(1 - \alpha|\hat{y}|)^{3/2} = \xi - \xi_{\max}, \tag{28}$$

where $\xi_{\max}$ is when the electron is at $\max(|\hat{y}|) = 1/\alpha$. It takes quarter of the period for the electron to go from $\hat{y} = 0$ to $\hat{y} = 1/\alpha$, and we can use that to estimate the period $\hat{T}_3$ from Eq. (28) to be

$$\hat{T}_3 \propto \frac{\zeta \hat{\mathcal{E}}_{\text{pond}}^{1/2} C}{\hat{H}_3^{1/2} W_{\max}^{(-)}}. \tag{29}$$

Based on Eq. (29), the resonance overlap condition $\hat{\Omega}_3 < 1$ for the stochastic heating sets a limit on the energy of stochastic motion $\hat{H}_3 < \hat{D}^2C^3/W_{\max}^{(-)}$, which exceeds $\hat{\mathcal{E}}_{\text{pond}}$ if $\zeta > W_{\max}^{(-)}/C$. This condition can be easily satisfied since $W_{\max}^{(-)} \ll C$. We can use Eqs. (11) and (27) to estimate the energy change $\Delta\hat{H}_3$ during one oscillation of the electron in the presence of a laser as

$$\Delta\hat{H}_3 = \int_{\hat{y}_{\max}}^{\hat{y}} \frac{\partial \hat{H}_3}{\partial \xi}\frac{d\xi}{d\hat{y}}d\hat{y} \propto \left(\frac{\hat{H}_3 \zeta \hat{\mathcal{E}}_{\text{pond}}^2 C}{W_{\max}^{(-)}}\right)^{1/3}, \tag{30}$$

where we assumed that $\hat{H}_3 \gg \Delta\hat{H}_3 \gg \hat{\mathcal{E}}_{\text{pond}}$. The scaling of maximum energy of stochastic motion for $C \ll W_{\max}^{(-)}$ can be estimated from

$$K \approx \left|\frac{\partial \hat{T}_3}{\partial \hat{H}_3}\Delta\hat{H}_3\right| \sim \left[\frac{\hat{\mathcal{E}}_{\text{pond}}}{\max(\hat{H}_3)}\right]^{7/6}\left(\frac{\zeta C}{W_{\max}^{(-)}}\right)^{4/3} = 1 \tag{31}$$

to be

$$\max(\hat{H}_3) \propto \hat{\mathcal{E}}_{\text{pond}}\left(\frac{\zeta C}{W_{\max}^{(-)}}\right)^{8/7}, \tag{32}$$

where we used estimates (29) and (30).

We now determine what value of $C$ corresponds to the largest stochastic energy for given $a_0$ and $\hat{D}$ parameters. Using estimates (7) and (8), we express $W_{\max}^{(-)}$ as

$$W_{\max}^{(-)} = \frac{\kappa_U - \kappa_B}{8}\hat{D}^2 = \frac{a_0\hat{D}}{2\left(2 + a_0^2\right)}. \tag{33}$$

Combining estimate (33) with energy limits (26) and (32) gives

$$\max(\hat{H}_2) \propto \frac{a_0\hat{D}^{7/5}}{\left(2 + a_0^2\right)^{1/5}}, \tag{34}$$

$$\max(\hat{H}_3) \propto \frac{\left(2 + a_0^2\right)^{8/7}C^{9/7}}{a_0^{2/7}} \ll \frac{a_0\hat{D}^{9/7}}{\left(2 + a_0^2\right)^{10/7}}. \tag{35}$$

The analysis above neglects the following aspects of the laser-target interaction. The length $\hat{L}$ of the gaps was assumed infinite, while in practice the value of $\hat{L}$ may be insufficient to both establish $\hat{\mathbf{E}}_{\text{qs}}$ and $\hat{\mathbf{B}}_{\text{qs}}$ and let the electrons reach maximum energy. The analysis neglects the energy balance between the laser and electrons of plasma; meanwhile in reality the laser will decay and hence $a_0 = a_0(\hat{z})$. For the laser with vector potential $-a_0(\hat{z})\cos(\xi)$, $C$ may no longer be a constant of motion, and the associated change in $\zeta$ affects the energy scaling. Note that we also neglected the nanoplate size $\hat{d}$. Since the laser field is absent inside the nanoplate, nonzero $\hat{d}$ means that when the electron escapes into the nanoplate at some $\xi_{\text{in}}$ it leaves the nanoplate at $\xi_{\text{out}} \neq \xi_{\text{in}}$. This $\xi_{\text{out}} - \xi_{\text{in}}$ jump changes the value of $C$, and the associated change in $\zeta$ affects the energy scaling. We also neglect all collisional effects, which may become increasingly important if the electron passes through nanoplates multiple times. Collisions can change the magnitude of electron's momentum $\hat{p}$, primarily

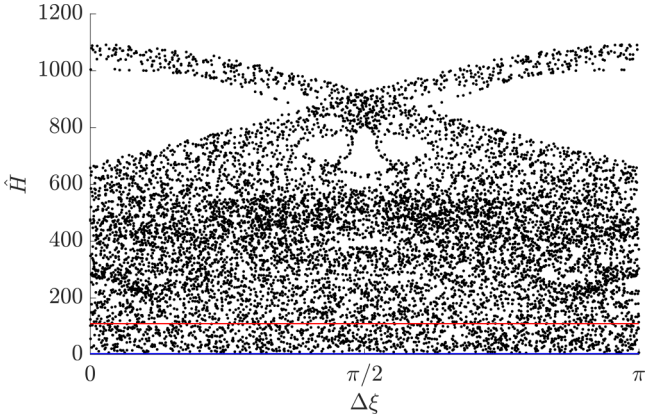


FIG. 4. Poincaré cross section for the electron with $C = W^{(-)}_{\max} = 2$, $W^{(+)}_{\max} = 5$, $\hat{y}(0) = 0.4\hat{D}$, $\hat{P}_y(0) = 3.0$, $\hat{D} = 500$. Parameters are chosen so that $\zeta = 1000$, and assumptions of analysis are satisfied. The motion is stochastic; however, a stability island exists for energies above 600. Red line at $\hat{H} \sim 100$ shows initial energy of the electron, and blue line at $\hat{H} = 7$ shows $W^{(+)}_{\max} + C$.

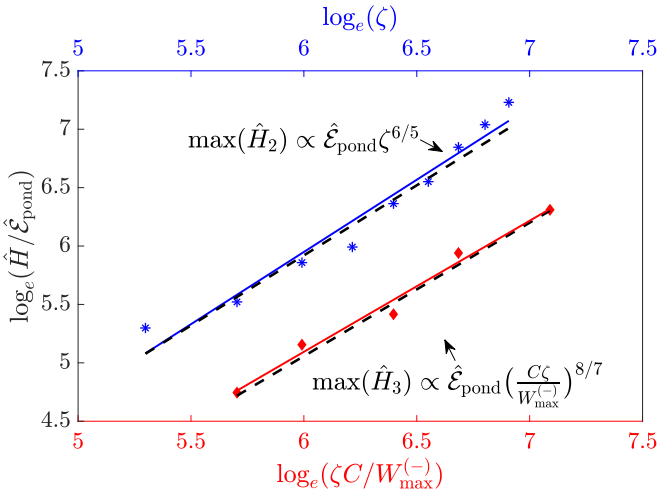


FIG. 5. Scaling of maximum stochastic energy for cases $C \sim W^{(-)}_{\max}$ [blue line corresponding to $\max(\hat{H}_2)$] and $C \ll W^{(-)}_{\max}$ [red line corresponding to $\max(\hat{H}_3)$], for various values of $\zeta$, $C$, and $W^{(-)}_{\max}$. Dashed lines show scalings (26) and (32) for reference.

due to the recoils from the electrons in the nanoplate. For relativistic electron $\hat{v}_z \sim 1$ the loss of momentum is negligible $\Delta\hat{p} \ll 1$ if [17]

$$\hat{d} \ll \frac{2\pi m^2 c^4}{\lambda n_e e^4 \ln\Lambda} \equiv \hat{d}_{\rm cl} \approx 30, \tag{36}$$

where $\ln\Lambda \sim 10$ is the Coulomb logarithm. For the setup described in Sec. II, $\hat{d} = 0.2\pi$, so requirement (36) is satisfied. Collisions with ions can scatter the electron, which also breaks conservation of $C$. A relativistic electron can penetrate into the ion's electron cloud and interact with the unshielded nucleus [18]; therefore the scattering cross section is $\sigma \propto Z_{\rm n}^2 e^4/(\gamma-1)^2 m^2 c^4$, where $Z_{\rm n}$ is the charge of the ion's nucleus. The effect of such collisions can be neglected if the electron's mean-free path $(\sigma n_i)^{-1}$ exceeds the nanoplate's width $d$, giving condition $\hat{d} \ll (\gamma-1)^2 \hat{d}_{\rm cl}/Z_{\rm n}$, which is satisfied for relativistic electrons with $\gamma \gtrsim 6$ in the solid copper target with $\hat{d} = 0.2\pi$.

In Sec. V we will show that despite the mentioned neglected aspects, the analysis of stochastic electron motion can explain the generation of high-energy electrons in our PIC simulations.

### A. Numerical verification

Analysis from Sec. IV is verified with a series of single-particle simulations. In these simulations, we vary setup parameters $a_0$, $\hat{D}$, $W^{(-)}_{\max}$, and $W^{(+)}_{\max}$ and the initial conditions of the electron $\hat{y}(0)$, $\hat{P}_y(0)$, $C$. Initial conditions are chosen so that the assumption (16) is satisfied at the beginning of the simulation. We run simulations for several $\zeta$, changing $\zeta$ between simulations by changing the $a_0$, $\hat{D}$, and $C$ parameters. We examine the Poincaré cross section of the electron trajectory, showing the electron's energies when the electron crosses $W^{(+)}(\hat{y}) = 0$ versus corresponding laser phase $\xi$ modulo $\pi$, that is, $\xi - [\xi, \pi]$, as in Fig. 4. Poincaré cross sections allow distinguishing stochastic and quasiperiodic electron motion because, for quasiperiodic motion, a Poincaré cross section shows smooth curves of preserved KAM surfaces. Some Poincaré cross sections still have preserved KAM surfaces (smooth arms at larger energies in Fig. 4). For these cases, we consider the maximum of $\hat{H}$ below the stability islands. The scalings from single-particle simulations match (26) and (32), as shown in Fig. 5.

## V. SIMULATION RESULTS AND DISCUSSION

Here we present our PIC simulation results and compare them to the analytical models from previous sections.

### A. *x*-polarized laser

To show how the $x$-polarized laser propagates into the target, we consider the setup with a normalized laser amplitude $a_0 = 2.4$ and gaps between nanoplates $\hat{D} = 4\pi$. From the PIC simulation of that setup, we plot the components of electric and magnetic fields, and compare them to our analytical model from Sec. II A. We choose $\hat{t} = 22\pi$, when roughly half of the laser pulse has passed the gap entrance at $\hat{z} = 0$. The $x$-component of the electric field $\hat{E}_{\rm x}$ is shown in Fig. 6, where the top subplot shows data from PIC, and the bottom subplot shows an analytical prediction. Likewise, the $z$-component of the magnetic field $\hat{B}_{\rm z}$ is shown in Fig. 7. Note that the model proposed in Sec. II A does not deal with electrodynamics of plasma and does not consider any specific relativistic effects. Despite its primitivity, the model captures the structure of $\hat{E}_{\rm x}$ from the relativistic PIC simulation.

In Sec. II A we predicted that the $x$-polarized pulse will not extract as many electrons as the $y$-polarized pulse will from the same target. In order to compare the density of extracted electrons, we plot the density of electrons from our PIC simulation in Fig. 8. In agreement with Sec. II A, PIC simulations show that the $x$-polarized pulse heats electrons less efficiently than the $y$-polarized pulse, as demonstrated in Fig. 13 below.

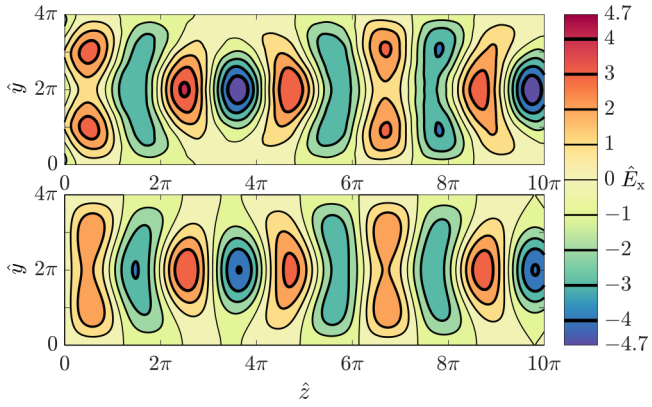


FIG. 6. The $x$-component of the electric field $\hat{E}_x$ inside the gap of size $\hat{D} = 4\pi$, obtained from PIC simulation (top) with an $x$-polarized laser and analytical model from Sec. II A (bottom).

### B. $y$-polarization

In Sec. III we demonstrated that when the $y$-polarized pulse propagates between nanoplates, it extracts some of the electrons. To illustrate the process of electron extraction, we consider the setup with $a_0 = 2.4$ and $\hat{D} = 4\pi$. From the PIC simulation of this setup, we plot the electron density between two nanoplates at time $\hat{t} = 22\pi$, as shown in Fig. 9. Note that electron extraction from the same target was also considered in Fig. 8. Simulation data presented in Figs. 8 and 9 show that the $y$-polarized laser extracts more electrons than the $x$-polarized does from the same target, in agreement with the analysis from Sec. II A. Our analysis presented in Sec. III suggests that extraction of electrons from the nanoplates leads to creation of quasistatic electric $\hat{\mathbf{E}}_{qs}$ and magnetic $\hat{\mathbf{B}}_{qs}$ fields. We now verify this prediction with our PIC simulation. To get the static components of $\hat{\mathbf{E}}$ and $\hat{\mathbf{B}}$ fields in the PIC simulation, we time-average these fields over one laser period $\hat{T}$. We use the $y$-component of the time-averaged electric field $\langle\hat{\mathbf{E}}\rangle \equiv \hat{\mathbf{E}}_{qs}$ to calculate the scalar potential $\hat{U}^{\rm PIC}$ defined as $\langle\hat{E}_y\rangle = d\hat{U}^{\rm PIC}/d\hat{y}$, and $z$-component of the time-averaged magnetic field $\langle\hat{\mathbf{B}}\rangle = \hat{\mathbf{B}}_{qs}$ to calculate the vector potential $\hat{A}_B^{\rm PIC}$ defined as $\langle\hat{B}_z\rangle = d\hat{A}_B^{\rm PIC}/d\hat{y}$. The magnitude of $\langle\hat{E}_y\rangle$ is largest

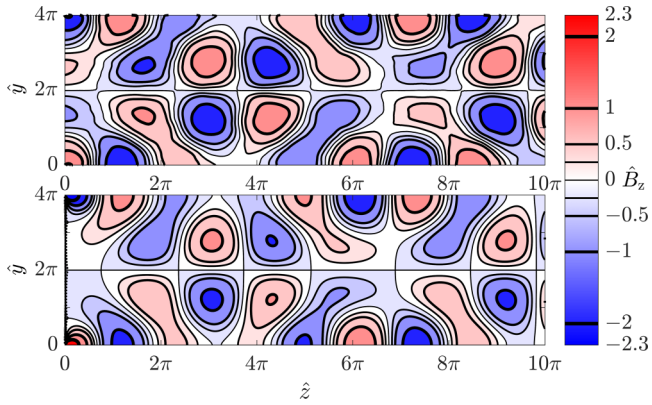


FIG. 7. The $z$-component of the magnetic field $\hat{B}_z$ inside the gap of size $\hat{D} = 4\pi$, obtained from the PIC simulation (top) with the $x$-polarized laser and analytical model from Sec. II A (bottom).

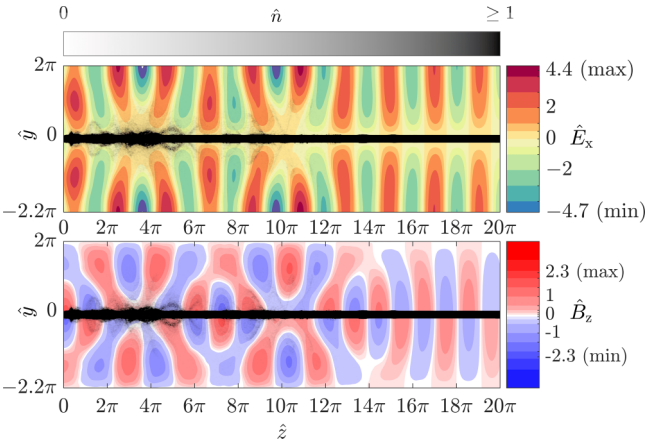


FIG. 8. Electron number density, overlaid with the components of electric $\hat{E}_x$ and magnetic $\hat{B}_z$ fields for the case of an $x$-polarized pulse.

near the nanoplates where $|\langle\hat{E}_y\rangle| \approx a_0$, as predicted in Sec. III. Profiles of $\hat{U}^{\rm PIC}$ and $\hat{A}_B^{\rm PIC}$ from PIC simulations with $a_0 = 2.4$ and different gap sizes $\hat{D}$ are shown in Fig. 10. In agreement with the analysis in Sec. III, electrons extracted from targets with larger $\hat{D}$ travel farther along the $z$-axis before mixing and creating homogeneous electron density, and hence for targets with larger $\hat{D}$ parabolic $U^{\rm PIC}$ and $A^{\rm PIC}$ potentials are formed at larger $\hat{z}$. We note that Fig. 10 includes the cases of $\hat{D} = 12\pi$, $16\pi$, and $24\pi$, where the length $\hat{L} = 40\pi$ was insufficient for the parabolic potentials to form. In PIC simulations with $a_0 = 2.4$ and $\hat{D} < 8\pi$, the $\hat{U}^{\rm PIC}$ and $\hat{A}_B^{\rm PIC}$ potentials are approximated well by a parabolic curve. In agreement with our analysis, parabolic potentials scale with the gap size $\hat{A}_B^{\rm PIC}$, $\hat{U}^{\rm PIC} \propto \hat{D}$. The estimate for static electric and magnetic fields neglects aspects such as the $z$-dependence of $a(z)$ laser potential due to absorption of laser energy by the target; however, the derived scalings for $\max(\hat{U})$ and $\max(\hat{A}_B)$ match reasonably well with the analysis. Specifically, for simulations with $a_0 = 2.4$, Eqs. (8) and (9) predict scaling $\max(\hat{U}) = a_0\hat{D}/4 = 0.6\hat{D}$, while the scaling in PIC simulations is $\max(\hat{U}) \propto 0.4\hat{D}$

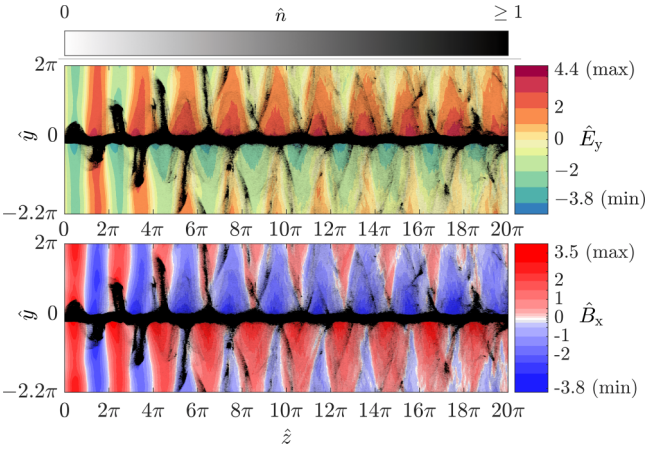


FIG. 9. Electron number density, overlaid with the components of electric $\hat{E}_y$ and magnetic $\hat{B}_x$ fields for the case of the $y$-polarized pulse.

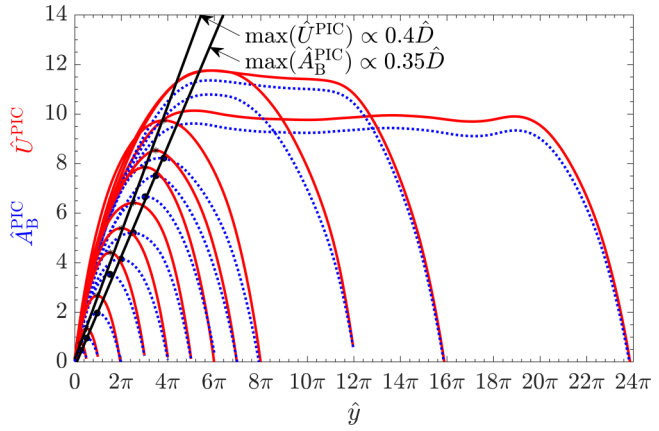


FIG. 10. Profiles of the electrostatic potential $\hat{U}^{\rm PIC}$ (red solid lines) and vector potential $\hat{A}_{\rm B}^{\rm PIC}\mathbf{e}_z$ (blue dotted lines). Each $\hat{U}^{\rm PIC}$ and $\hat{A}_{\rm B}^{\rm PIC}\mathbf{e}_z$ is shown from $\hat{y}=0$ to $\hat{y}=\hat{D}$, where $\hat{D}$ is the gap size from corresponding PIC simulation. All PIC simulations shown had the same laser with $a_0 = 2.4$.

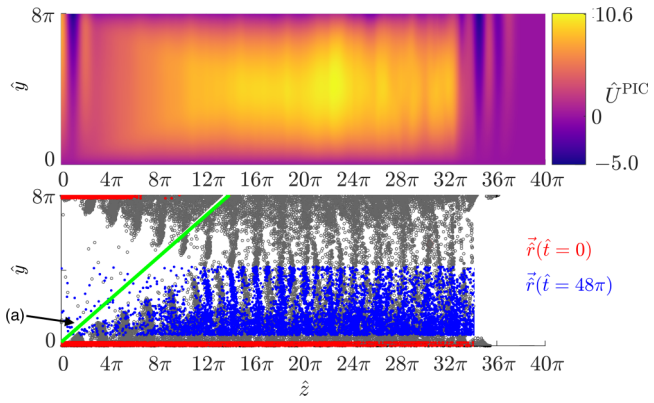


FIG. 12. Top panel shows scalar potential $\hat{U}^{\rm PIC}$ inside the gap from a PIC simulation with $a_0 = 2.4$, $\hat{D} = 8\pi$, at time $\hat{t} = 48\pi$. Bottom panel shows positions of the electrons from the random subset (light gray dots) sampled in the same PIC simulation at time $\hat{t} = 48\pi$. Extracted electrons fill the region of the gap with $\hat{z}$ from $12\pi$ to $32\pi$; the same region has the $\hat{U}^{\rm PIC}$ and $\hat{A}_{\rm B}^{\rm PIC}$ independent of $\hat{z}$. Green line marked (a) shows the extraction angle estimate (6). In the bottom panel, red points (dark gray if grayscale) at $\hat{D}=0$ and $8\pi$ show the initial position $\vec{r}(\hat{t}=0)$ of the electrons that are located between $\hat{D}=0$ and $4\pi$ at time $\hat{t}=48\pi$.

as shown in Fig. 10. The $\max(\hat{U}) = |\hat{v}_z|\hat{A}_{\rm B}$ estimate agrees well with the series of simulations presented in Fig. 11, where we varied $a_0$ while keeping $\hat{D} = 2\pi$ and tracked the subset of electrons to determine the average velocity component $\langle\hat{v}_z\rangle$ in the gaps of the target. Results shown in Fig. 11 also confirm that $\langle\hat{v}_z\rangle$ increases with $a_0$, even though the values of $\langle\hat{v}_z\rangle$ for larger $a_0$ are the smaller estimate (7), and therefore the ponderomotive $\langle\hat{v}_z\rangle$ estimate becomes less adequate in the presence of larger $\hat{U}$ and $\hat{A}_{\rm B}$ potentials. For the $a_0 = 2.4$, estimate (7) gives $\langle\hat{v}_z\rangle = 0.74$, which agrees with $\hat{v}_z^{\rm PIC} = 0.73$ recorded in a PIC simulation with $\hat{D} = 2\pi$. The main conclusion regarding quasistatic $\hat{\mathbf{E}}_{\rm qs}$ and $\hat{\mathbf{B}}_{\rm qs}$ fields is that their corresponding potentials $\hat{U}$ and $\hat{A}_{\rm B}\mathbf{e}_z$ are indeed parabolic if the depth $L$ is sufficient and $|\hat{U}| = |\hat{v}_z\hat{A}_{\rm B}|$, hence there is a residual $W_{\rm max}^{(-)}$ always present.

Having confirmed the onset of quasistatic $\hat{\mathbf{E}}_{\rm qs}$ and $\hat{\mathbf{B}}_{\rm qs}$ fields and the residual between them, we now consider the acceleration of electrons in our PIC simulations to verify

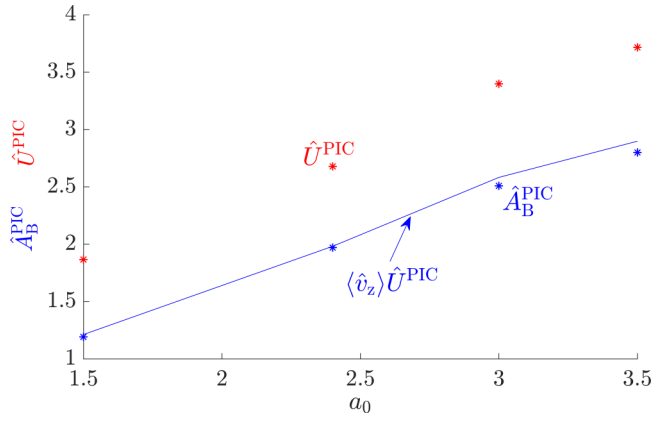


FIG. 11. Maximum values of scalar $\max(\hat{U}^{\rm PIC})$ and vector $\max(\hat{A}_B^{\rm PIC})$ agree with the estimate $\max(\hat{A}_{\rm B}^{\rm PIC}) = \langle v_z\rangle \max(\hat{U}^{\rm PIC})$, where $\langle v_z\rangle$ is the average $v_z$ velocity component of the electrons in the gap.

the analysis presented in Sec. IV. To demonstrate when the problem setup considered in Sec. IV becomes relevant to our PIC simulations, consider an example from the PIC simulation with $a_0 = 2.4$ and $\hat{D} = 8\pi$, shown in Fig. 12, where we plot the subset of electrons between two nanoplates at time $\hat{t} = 38\pi$. As Fig. 12 shows, the profiles of $\hat{U}^{\rm PIC}$ and $\hat{A}_{\rm B}^{\rm PIC}$ remain constant with $\hat{z}$ after $\hat{z}\gtrsim 12\pi$, where the electrons have filled the gap. Therefore, electrons with $\hat{z}\gtrsim 12\pi$ shown in Fig. 12 are relevant to the analysis form Sec. IV. We note that in the setup considered in Sec. IV, $C$ of the electron is conserved, while in PIC simulation, $C$ can change prior to formation of quasistatic fields, and also in the quasistatic fields via mechanisms discussed at the end of Sec. IV. Since the immobile electron has $C \sim 1$, it is reasonable to assume that majority of electrons will have $C \sim 1$ when the quasistatic field is established. Furthermore, if the residual between the quasistatic electric and magnetic field corresponds to $W_{\rm max}^{(-)} \sim 1$, then there will be electrons with $C \sim W_{\rm max}^{(-)}$ that can undergo efficient stochastic acceleration. As the electrons undergo stochastic acceleration, the density in the gap $\langle n\rangle$ and the average velocity $\langle\hat{v}_z\rangle$ remains unchanged, so the quasistatic electric and magnetic fields also stay the same. Our next step is to show that the low-energy electrons with $C$ closest to $W_{\rm max}^{(-)}$ can heat up the most efficient and that their maximum stochastic energy matches the maximum energy in PIC simulations. We start by finding the maximum electron energy $\gamma_{\rm max}^{\rm PIC}$ in PIC simulations from the energy distribution functions $f(\gamma)$, as shown in Fig. 13. Then we use the $\hat{U}^{\rm PIC}$ and $\hat{A}_{\rm B}^{\rm PIC}$ from each simulation to study the electron heating in a single-particle model. For the $\hat{U}^{\rm PIC}$ and $\hat{A}_{\rm B}^{\rm PIC}$ potentials, we calculate how the unperturbed frequency $\hat{\Omega}(C)$ changes with $C$ for the electron with $\gamma_{\rm max}^{\rm PIC}$. The $\hat{\Omega}(C)$ dependencies shown in Fig. 14 show that $C \ll 1$ electrons have $\hat{\Omega} \gg 1$ and therefore are unable to exchange energy with the laser efficiently. The frequency $\hat{\Omega}$ drops to $\hat{\Omega} < 1$ in a narrow region of $C \approx W_{\rm max}^{(-)}$. This $C \approx W_{\rm max}^{(-)}$ also corresponds to

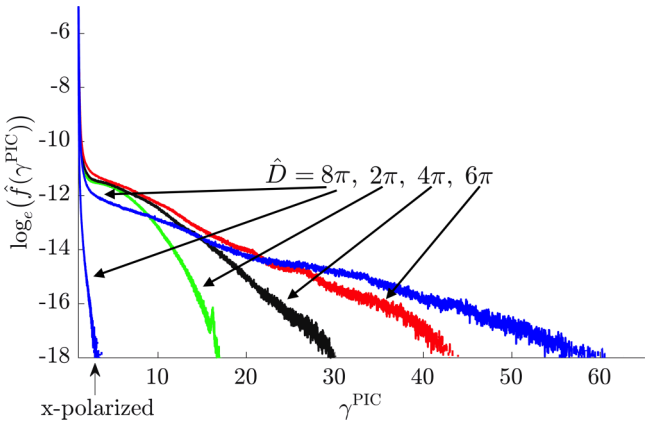


FIG. 13. Distribution of an electron's Lorentz factor $\gamma$ normalized by the total number of particles in the target ($\sim 10^{10}$ taking the size along $x$ as $\Delta x \sim \lambda$ and size along $y$ as $\Delta y \sim d + D$) for PIC simulations with $a_0 = 2.4$ and different $\hat{D}$. The corresponding values of $\hat{D}$ are $2\pi$ (green), $4\pi$ (black), $6\pi$ (red), $8\pi$ (blue). Data shown for the $x$-polarized $\hat{D} = 8\pi$ verify that $x$-polarized pulse heats up electrons less efficiently, in agreement with Sec. II A.

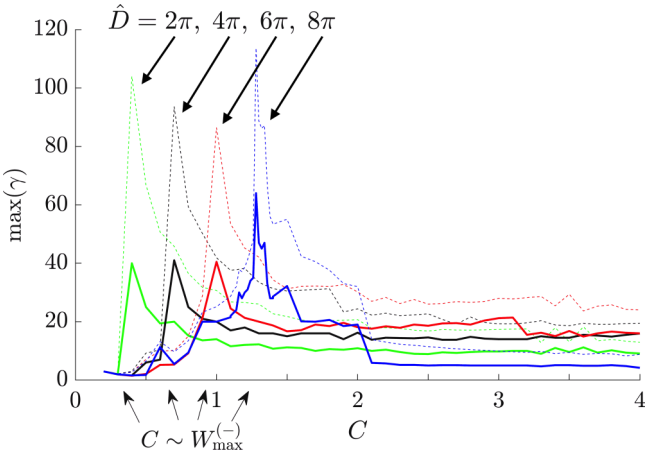


FIG. 15. The maximum energy (dashed curves) and energy below stability arms (solid curves) from single-particle simulations with initial $\hat{H} \sim 1$ and for scalar $\hat{U}$ and vector $\hat{A}_{\rm B}\mathbf{e}_z$ potentials from PIC simulations with $a_0 = 2.4$ and $\hat{D} = 2\pi$ (green), $4\pi$ (black), $6\pi$ (red), $8\pi$ (blue).

the maximum stochastic energy recorded in the single-particle simulation, as shown in Fig. 15. Our analysis showed that the maximum stochastic energy $\max(\hat{H})$ surpasses the ponderomotive energy $\hat{\mathcal{E}}_{\rm pond}$ for electrons with $\zeta \gtrsim 1$ and scales as $\max(\hat{H}) \propto \hat{\mathcal{E}}_{\rm pond}\zeta^{6/5}$. The scaling from PIC results shown in Fig. 16 is $\max(\hat{H}) \propto \hat{\mathcal{E}}_{\rm pond}\zeta^{0.98}$.

Apart from the maximum energy, hot electron bunches are also characterized by assigning them a temperature or considering the heat flux of electrons [19]. To characterize the mean energy of electrons, we determine the energy $\hat{\mathcal{E}}_{\rm mean}$ at which half of the electron's heat flux is captured. In the series of PIC simulations shown in Fig. 16, the scaling of mean electron energy is $\max(\hat{\mathcal{E}}_{\rm mean}) \propto a_0^2\zeta^{0.8}$.

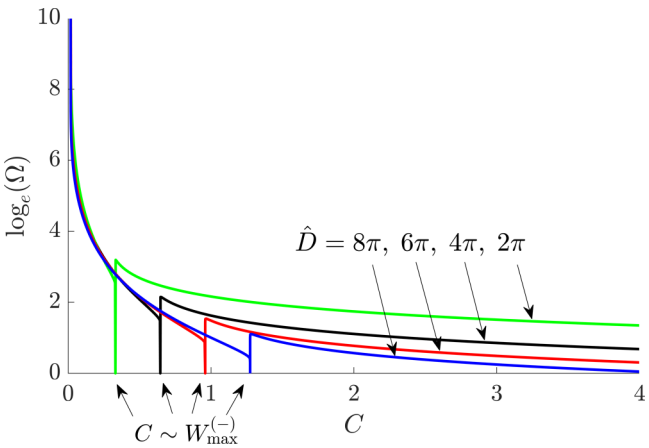


FIG. 14. The frequency of unperturbed electron motion $\hat{\Omega}$ for scalar $\hat{U}$ and vector $\hat{A}_{\rm B}\mathbf{e}_z$ potentials measured in PIC simulations with $a_0 = 2.4$ and $\hat{D} = 2\pi$ (green), $4\pi$ (black), $6\pi$ (red), $8\pi$ (blue). Dotted lines show $C \approx W^{(-)}_{\rm max}$, where $\hat{\Omega}$ drops to zero.

## VI. CONCLUSION

In this paper, we investigated various aspects of laser interaction with a 2D nanoplate array target. It showed that the target behaves much like a waveguide for the laser propagation: for the $x$-polarized pulse, the plane wave laser pulse becomes a superposition of TE-modes, whereas, for a $y$-polarized pulse, the laser propagates as a TEM mode. The analysis showed that for an $x$-polarized laser, the ponderomotive force from the EM fields would prevent the extraction of electrons from the target. As a result, electrons remain in the target and do not interact with the laser field. The electron acceleration is suppressed, which has been confirmed by the PIC simulations, which show that the maximum electron energies for an $x$-polarized pulse are lower than those for a $y$-polarized pulse. On the other hand, the $y$-polarized laser pulse, propagating between the nanoplates while preserving the plane-wave

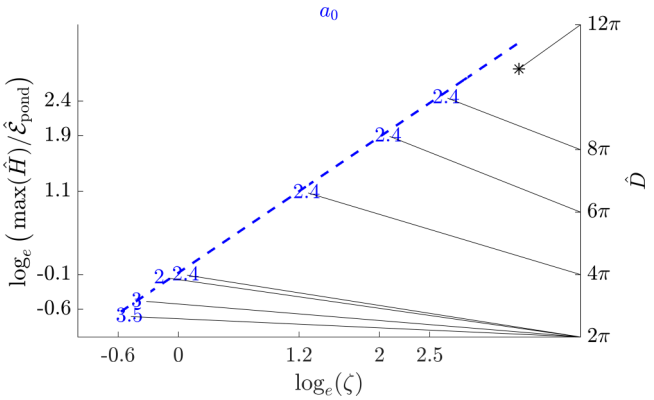


FIG. 16. The energy scaling in the PIC simulations with $W^{(-)}_{\rm max} \sim 1$. Data are labeled with blue numbers, corresponding to the values of $a_0$ in PIC simulations. The fitted slope is 0.98. The black star that does not fit the scaling corresponds to the simulation with $a_0 = 2.4$ and $\hat{D} = 12\pi$, where $\hat{L} = 20$ turned out to be insufficient for the electrostatic potentials to form.

structure, can pull electrons out from the nanoplates due to the Lorentz force from its electric field. This extraction of electrons can be described well by the motion of a single electron in a plane wave, where the laser pulse can extract bunches of electrons from their parent nanoplates. Electron bunches streaming along and against the $y$-axis are shifted in the $z$-axis direction by the laser phase $\Delta\xi = \pi$. As a result, when these counterpropagating bunches pass through each other, they form homogeneous electron density $\hat{n}$ depending on the laser amplitude $a_0$ and gap depth $\hat{D}$ and thus create a quasistatic electric field $\hat{\mathbf{E}}_{\rm qs}$ in the $y$-direction. Simultaneously, the electrons in the gap move along the $z$-axis, and thus their current generates a quasistatic magnetic field $\hat{\mathbf{B}}_{\rm qs}$ in the $x$-direction. Our estimates for the quasistatic EM fields suggest that $|\hat{\mathbf{E}}_{\rm qs}| = |\hat{v}_z\hat{\mathbf{B}}_{\rm qs}|$, where $\hat{v}_z$ is the averaged longitudinal speed of extracted electrons. Therefore, the quasistatic magnetic field is relatively smaller than the electric field. In contrast to the ion-channel case, we showed that this small difference in these quasistatic fields is crucial for the electron acceleration beyond the ponderomotive scaling.

After the formation of these quasistatic fields, the new injected electrons in the gap can be accelerated via the resonance between the frequency of electron oscillating in the quasistatic fields and laser frequency. We show that the electron can be accelerated via the stochastic motion, which we study within the 3/2D Hamiltonian framework. Our analysis shows that the electron energy can largely exceed the ponderomotive energy scaling due to the onset of stochastic motion, which depends on an universal parameter $\zeta$ combining the laser amplitude $a_0$, gap size $\hat{D}$, and initial electron conditions. We found that the stochastic motion requires $\zeta > 1$, which can be easily satisfied for our PIC simulations. The analysis demonstrated that for larger gap depth $\hat{D}$, the stochastic motion results in larger electron energy. However, if the laser amplitude increases, even though the maximum electron energy is enhanced, its ratio to the ponderomotive scaling is decreased. In particular, if the laser amplitude is large enough that $\zeta \lesssim 1$, then the stochastic motion is not possible, and the maximum electron energy will be the same order with ponderomotive scaling.

We note that the process of electron acceleration in laser-particle interaction is more complex than the simple model we considered, but our analysis explains how the energetic electrons will be produced in laser-target interaction via the stochastic electron motion. The presented analysis can help with interpreting the results of both future experiments and simulations.

## ACKNOWLEDGMENT

This work was supported by the University of California Office of the President Lab Fee Grant No. LFR-17-449059.

[1] M. Murnane, H. Kapteyn, S. Gordon, J. Bokor, E. Glytsis, and R. Falcone, Appl. Phys. Lett. **62**, 1068 (1993).
[2] M. A. Purvis, V. N. Shlyaptsev, R. Hollinger, C. Bargsten, A. Pukhov, A. Prieto, Y. Wang, B. M. Luther, L. Yin, S. Wang *et al.*, Nat. Photonics **7**, 796 (2013).
[3] G. Kulcsar, D. AlMawlawi, F. W. Budnik, P. R. Herman, M. Moskovits, L. Zhao, and R. S. Marjoribanks, Phys. Rev. Lett. **84**, 5149 (2000).
[4] F. Khattak, R. Clarke, E. Divall, M. Edwards, P. Foster, C. Hooker, A. Langley, P. Mistry, D. Neely, O. P. du Sert *et al.*, EPL (Europhys. Lett.) **72**, 242 (2005).
[5] L. Fedeli, A. Formenti, L. Cialfi, A. Pazzaglia, and M. Passoni, Sci. Rep. **8**, 3834 (2018).
[6] J. Snyder, L. Ji, K. M. George, C. Willis, G. E. Cochran, R. Daskalova, A. Handler, T. Rubin, P. L. Poole, D. Nasir *et al.*, Phys. Plasmas **26**, 033110 (2019).
[7] Y. Zhang and S. Krasheninnikov, Phys. Lett. A **382**, 1801 (2018).
[8] Y. Zhang and S. Krasheninnikov, Phys. Plasmas **25**, 013120 (2018).
[9] Y. Zhang, S. Krasheninnikov, and A. Knyazev, Phys. Plasmas **25**, 123110 (2018).
[10] S. C. Wilks, W. L. Kruer, M. Tabak, and A. B. Langdon, Phys. Rev. Lett. **69**, 1383 (1992).
[11] C. Bargsten, R. Hollinger, M. G. Capeluto, V. Kaymak, A. Pukhov, S. Wang, A. Rockwood, Y. Wang, D. Keiss, R. Tommasini *et al.*, Sci. Adv. **3**, e1601558 (2017).
[12] D. Gozhev, S. Bochkarev, N. Busleev, A. Brantov, S. Kudryashov, A. Savel'ev, and V. Y. Bychenkov, High Energy Density Phys. **37**, 100856 (2020).
[13] T. Arber, K. Bennett, C. Brady, A. Lawrence-Douglas, M. Ramsay, N. Sircombe, P. Gillies, R. Evans, H. Schmitz, A. Bell *et al.*, Plasma Phys. Controlled Fusion **57**, 113001 (2015).
[14] L. D. Landau, J. Bell, M. Kearsley, L. Pitaevskii, E. Lifshitz, and J. Sykes, *Electrodynamics of Continuous Media*, Landau and Lifshitz Course of Theoretical Physics Vol. 8 (Elsevier, London, England, 2013).
[15] A. Arefiev, A. Robinson, and V. Khudik, J. Plasma Phys. **81** (2015).
[16] R. Z. Sagdeev, G. M. Zaslavsky, and D. A. Usikov, *Nonlinear Physics: From the Pendulum to Turbulence and Chaos* (Harwood, Chur, Switzerland, 1988).
[17] J. Connor and R. Hastie, Nucl. Fusion **15**, 415 (1975).
[18] E. J. Williams, Proc. R. Soc. London A **169**, 531 (1939).
[19] B. S. Paradkar, M. S. Wei, T. Yabuuchi, R. B. Stephens, M. G. Haines, S. I. Krasheninnikov, and F. N. Beg, Phys. Rev. E **83**, 046401 (2011).